Damage in duplex steels studied at mesoscopic and macroscopic scales

Léa Le Joncour, Benoît Panicaud, Andrzej Baczmanski, Manuel François,
Chedly Braham, Anna Maria Paradowska, Sebastian Wroński, Rémi Chiron

Damage in duplex steels studied at mesoscopic and macroscopic scales

L. Le Joncour [a], B. Panicaud [a,*], A. Baczmański [b], M. Francois [a], C. Braham [c], A. Paradowska [d], S. Wroński [b], R. Chiron [e]

[a] *Université de Technologie de Troyes (UTT), CNRS UMR 6279, 12 rue Marie Curie, 10010 Troyes, France*
[b] *Faculty of Physics and Applied Computer Science, AGH-University of Science and Technology, Al. Mickiewicza 30, 30-059 Kraków, Poland*
[c] *LIM, CNRS UMR 8006, Ecole Nationale Supérieure d'Arts et Métiers, 151 Bd de l'Hôpital, 75013 Paris, France*
[d] *Rutherford Appleton Laboratory (ISIS), Chilton Didcot, Oxfordshire OX11 0QX, UK*
[e] *LPMTM, Université Paris 13, 99, Av. J.-B. Clément, 93430 Villetaneuse, France*

ABSTRACT

Different experimental approaches have been performed in order to extract damage at several scales. In this paper two experimental methods are treated. Neutron diffraction coupled with tensile test has been performed to study damage at mesoscopic scale. At macroscopic scale, classical tensile test has been used to extract damage effects, from material hardening evolution. Optical measurements and particular data treatment have been used in order to correct data for the necking phenomenon at large deformation, for each experimental method. Damage process in duplex steels has then been analysed at both macroscopic and mesoscopic scales using scale transition models. Eventually, investigations at those scales have been compared to understand correlation between mesoscopic and macroscopic behaviour of our material.

1. Introduction

Nowadays, it is possible to develop numerical simulation for manufacturing processes in finite transformation. In order to improve the predictivity of finite elements analysis (FEA), it is necessary to provide accurate constitutive models for mechanical behaviour. Such a methodology is now classical. The aim of the present work is to develop experimental techniques and data treatments to study damage mechanisms for metallic materials. Indeed, it is now well known that the coupling between damage and plasticity leads to an accurate description of ductile damage in metal forming (Saanouni et al., 2000; Saanouni and Hammi, 2000; Lemaitre and Chaboche, 2001; Chaboche et al., 2006). In this paper, we have studied the

opportunity to measure the mechanical consequences of damage in duplex steels, at different scales. Therefore, two scales have been considered and a particular experimental approach has been performed. Neutron diffraction coupled with in situ tensile test has been used to study damage at mesoscopic scale. Classical tensile tests have also been used to obtain damage at macroscopic scale, from hardening evolution.

Firstly, diffraction methods for lattice strain measurements can provide useful information concerning the nature of grains behaviour during elastoplastic deformation. The advantage of diffraction methods is that measurements are performed selectively only for the crystallites contributing to the measured diffraction peak, i.e. for the grains having lattice orientations for which the Bragg condition is fulfilled (Greenough, 1949; Gloaguen et al., 2002a, 2002b). When several phases are present within a specimen, the measurements of separate diffraction peaks allow the investigation of each phase independently (Amos et al.,

1994; Fitzpatrick et al., 1997; Fréour et al., 2002, 2003, 2005; Quinta Da Fonseca et al., 2006; Dakhlaoui et al., 2006). Moreover, comparison of diffraction data with self-consistent model is very convenient to study elasto-plastic properties at mesoscopic and macroscopic scales. Analysis of experimental data using model predictions helps us to understand the physical phenomena which occur during sample deformation (Wierzbanowski et al., 1992; Fitzpatrick et al., 1997; Baczmanski et al., 2008). Besides, mesoscopic and macroscopic parameters of elastoplastic deformation can be then experimentally identified (Baczmański et al., 1999; Clausen et al., 1999).

Secondly, classical tensile loading is used to provide damage evolution at macroscopic scale (Cabezas and Celentano, 2004). Indeed, damage has been measured here from elastoplastic hardening evolution (Lemaitre and Chaboche, 2001; Hfaiedh, 2009). To extract damage occur-ring at macroscopic scale, it is necessary to take into account the necking phenomenon (Celentano and Chab-oche, 2007). This has been done using simultaneously opti-cal measurements for the cross-section and for the local strain within the necking area. Macroscopic models have been then used to compare with experimental results. Con-sequently, an inverse method has been applied to identify model parameters. Errors have been taken into account to analyse results from different macroscopic models. Even-tually, we have obtained different damage curves depend-ing from the data treatment considered and corresponding to different spatial parts of the sample.

In this paper, we present the experimental results from both techniques, and compare them in order to character-ize damage evolution of duplex stainless steels (DSS) which is of obvious interest for industrial applications in highly corrosive process, such as chemical, petrochemical, off-shore, nuclear or paper industries and are yet fre-quently studied (Chehab et al., 2010; Hedström et al., 2010).

Further data treatments and calculations are based on approximations and corrections, listed below and detailed in the later parts of the text.

(1) Whatever the scale, the experimental data are fitted with elastoplastic models without taking account damage. Damage is so extracted from fitting/com-parison process and is treated within the continuous damage mechanics (CDM).
(2) In calculations, the elastoplastic models take into account non-linear isotropic hardening and texture evolution. However, stress concentration and triaxi-ality of stains and stresses are neglected as discussed further.
(3) Necking effect has been corrected through optical measurements of sample cross-section. Grids are also used to measure local strain and a particular calibration was especially applied for diffraction results.

2. Material

The studied material is an austeno-ferritic stainless steel, containing approximately 50% austenite and 50% ferrite. It was obtained by continuous casting, and then hot rolled down to 15 mm sheet thickness. The sample was prepared from UR45 N steels which chemical compo-sition is given in Table 1. The characteristic microstructure of this steel consists of austenitic islands elongated along the rolling direction and embedded in a ferritic matrix. EBSD method has shown that all crystallites of ferritic phase have almost the same orientation, while austenitic islands are divided into smaller grains with different orien-tations of the lattice (Baczmański and Braham, 2004; Dakhlaoui et al., 2006; Baczmański et al., 2008). The sam-ple (designated as UR45 N) was annealed during 1000 h at a temperature of 400 °C and next cooled in ambient air. It is well known (Lacombe et al., 1990; Mateo et al., 1997; Park and Kwon, 2002) that, at this temperature of ageing (lower than 475 °C), the decomposition of ferrite by the mechanism of spinodal decomposition occurs. Transformations in ferrite are mainly decomposition of $\tilde{\alpha}/\tilde{\alpha}'$ (into Cr-poor $\tilde{\alpha}$ and Cr-rich $\tilde{\alpha}'$ domains) and precipi-tation of an intermetallic phase rich in Ni, Si and Mo (the G phase). The role of $\tilde{\alpha}'$ and the G phases in hardening and embrittlement of ferrite is widely discussed in the lit-erature and the majority of authors (Marcinkowski et al., 1964; Lagneborg, 1967) agree that hardening is attributed essentially to the $\tilde{\alpha}'$ phase. Indeed, the coherence shift be-tween the lattice parameters of $\tilde{\alpha}$ and $\tilde{\alpha}'$ phases introduces internal stresses reducing the dislocations mobility. The G particles have very small size (between 1 and 10 nm gen-erally and up to 50 nm occasionally) and they precipitate, more or less uniformly, in the ferritic grains depending on the chemical composition of steels. The largest particles are formed preferentially in defects: the others are formed in the $\tilde{\alpha}/\tilde{\alpha}'$ and austenite/ferrite interfaces. Some micro-structural transformations may be present in the austenitic phase but they do not change mechanical properties of the material.

3. Experimental methods at mesoscopic scale

3.1. Measurements by neutron diffraction

The ENGIN-X diffractometer (Santisteban et al., 2006) was used to measure interplanar spacings $\langle d \rangle_{\{hkl\}}$ using time-of-flight (TOF) neutron diffraction method at the ISIS spallation neutron source. The experimental setup consists of two detector banks which are centred on horizontal scattering angles of 2 = ±90° (Fig. 1). The detectors measure time-resolved spectra, each Bragg peak being produced by reflections from a different family of {hkl} planes.

The sample shown in Fig. 1 with an initial diameter of 8 mm, having axis aligned along rolling direction (RD) was machined from UR45 N steels. The lattice strains were "in situ" measured during uniaxial tensile loading. The load axis was aligned horizontally at +45° to the incident beam,

Table 1
Chemical composition of duplex stainless steel: mass-percent.

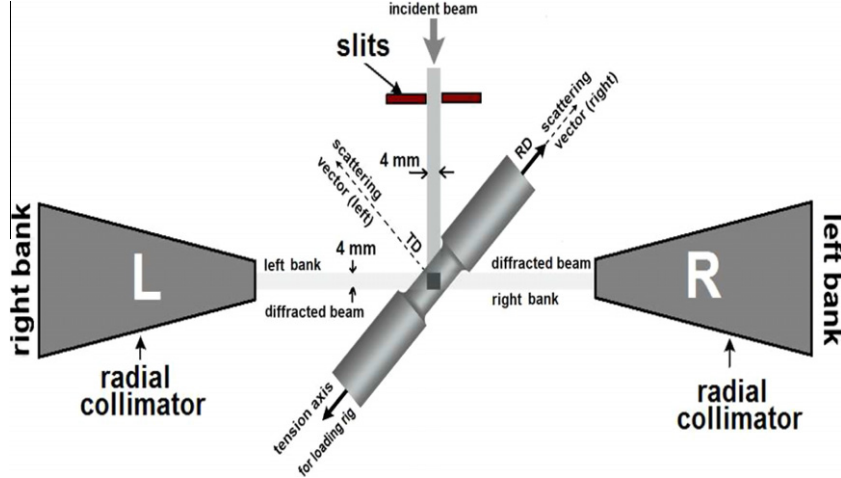|	C	Mn	Cr	Ni	Mo	Cu	S	N
UR45 N	0.015	1.6	22.4	5.4	2.9	0.12	0.001	0.17

Fig. 1. Experimental setup for measurements of initial phase stresses and orientation of the scattering vector, with respect to the sample frame during measurements. The neutron gauge volume is: $4 \times 4 \times 8$ mm, where 8 mm is the beam size in perpendicular direction.

allowing simultaneous measurements of lattice strains in both directions: parallel and perpendicular to the applied load (Fig. 1). A slit of dimensions 8 mm high, 4 mm wide was used to define the incident beam. Radial collimators in front of each detector bank defined an exit aperture of approximately 4 mm (Fig. 1). The measurements were made at a series of applied strains after stabilisation of the load subjected to the sample. The strains (monitored for small deformation by an extensometer) were held constant during the measurement intervals. The experiments were performed using the TOF diffraction method and the peak positions for several {hkl} reflections were determined independently for both phases using a least square fitting procedure based on theoretical pseudo-Voigt function (François et al., 2000; Courant et al., 2000; Hutchings et al., 2005; Pecharsky et al., 2008). The interplanar spacings $\langle d_{RD} \rangle_{\{hkl\}}$ were then determined. The relative elastic lattice strains $\langle \epsilon_{RD} \rangle_{\{hkl\}}$ with respect to the initial interplanar spacings were calculated for different {hkl} reflections of the scattering vector:

$$\langle \varepsilon_{RD}^{elastic} \rangle_{\{hkl\}} = \ln \left(\frac{\langle d_{RD}^{\Sigma} \rangle_{\{hkl\}}}{\langle d_{RD}^{0} \rangle_{\{hkl\}}} \right), \qquad (1)$$

where $\langle d_{RD}^{\Sigma} \rangle_{\{hkl\}}$ and $\langle d_{RD}^{0} \rangle_{\{hkl\}}$ are the interplanar spacings measured for a sample with and without external load; while the $\langle \ \rangle_{\{hkl\}}$ brackets denote the average over the volume of diffracting grains for which the scattering vector is perpendicular to the {hkl} planes. The subscript RD indicates the direction of interplanar spacings and strain measurements, i.e. the direction of scattering vectors.

3.2. Necking correction for the stresses

A stress correction has been performed by an original calibration in order to take into account the necking effect, shown in Fig. 2 (Le Joncour et al., 2010). To perform this calibration in the neutron gauge, it is assumed that the real macroscopic stress $\sum_{RD}$ (average over the neutron gauge) is proportional to the mean elastic strain $\langle \varepsilon_{RD}^{elastic} \rangle_{mean}$ (arithmetic average on measured lattice strain $\langle \varepsilon_{RD}^{elastic} \rangle_{\{hkl\}}$), not only in the elastic stage but also for large plastic deformation and is assumed correct even when some damage phenomena occur. In this approximation, the influence of interphase or intergranular stresses on the mean strain value $\langle \varepsilon_{RD}^{elastic} \rangle_{mean}$ is neglected (Fréour et al., 2003). This is because $\langle \varepsilon_{RD}^{elastic} \rangle_{mean}$ is calculated over the volume
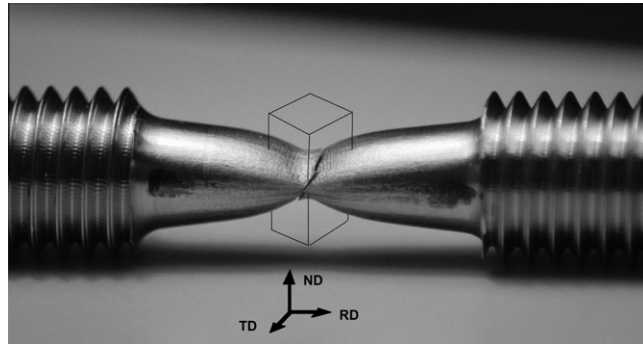

Fig. 2. Aged UR45 N sample broken in tensile test (orientation and position of the neutron gauge volume with respect to the neck is shown). Note the strong strain anisotropy between TD and ND.

containing a large number of grains belonging to both phases and having different orientations. In such volume the intergranular stresses integrated over both phases sum approximately to zero value. To support our previous assumption the evolution of the theoretical strain $\langle \varepsilon_{RD}^{elastic} \rangle_{mean}$ during elastoplastic deformation was calculated using elastoplastic self-consistent model (Baczmanski and Braham, 2004). The results shown in Fig. 3 confirm that a linear relation exists between the theoretical macroscopic stress and the mean strain $\langle \varepsilon_{RD}^{elastic} \rangle_{mean}$ for whole range of elastoplastic deformation, whatever the inclusion geometry.

To calibrate the experimental results, the relation between the mean strain $\langle \varepsilon_{RD}^{elastic} \rangle_{mean}$ and the macroscopic stress must be established. It was done using the linear elastic range of the function $\sum_{RD}^{apl}$ vs. $\langle \varepsilon_{RD}^{elastic} \rangle_{mean}$ (up to $\sum_{RD}^{apl} = 200$ MPa) and next the linear function was extrapolated for all values of $\langle \varepsilon_{RD}^{elastic} \rangle_{mean}$. Using this calibration curve (Fig. 3), the values for macroscopic stress in the neutron gauge (i.e., $\sum_{RD}^{cor}$ corrected) can be then easily calculated from the mean strain $\langle \varepsilon_{RD} \rangle_{mean}$ for all experimental points. It should be stated that the experimental calibration curve ($\sum_{RD}^{cor}$ vs. $\langle \varepsilon_{RD} \rangle_{mean}$) is very close to the theoretical relation obtained by the self-consistent model (Fig. 3).

In the presented above calibration method, it was assumed that the elastic properties of grains and of the polycrystalline aggregates are constant during elastoplastic deformation and also during damage stage. However, it has been shown (Lemaitre and Chaboche, 2001) that damage can influence the value of effective elastic modulus. Consequently, this calibration has to be performed carefully until the end of tensile tests, when macroscopic damage becomes more significant, in order to minimize errors.

Comparisons with numerical modelling have also been performed. The interpretation of neutron diffraction results is based on an elastoplastic self-consistent model developed by Lipinski and Berveiller (1989) and applied for neutron measurements on duplex steel by Baczmański et al. (2003, 2004) The calculations are performed on two

different scales: the macroscopic scale, where the average quantities (Σ, E) are defined, and the (mesoscopic) grain scale, on which the behaviour of each crystallite under mesoscopic stress σ is described (Le Joncour et al., 2010). This allows comparing directly the measured elastic lattice strain with the theoretical values. Results of comparison are presented in Fig. 4, where a good correlation between the self-consistent model and the experimental points until damage process is shown. The agreement of model and experimental data also justifies the previous calibration of the macroscopic stress values. As mentioned in introduction part, damage process is not taken into account in these self-consistent calculations.

3.3. Treatment of experimental data and mesoscopic damage calculations

As stated above, the triaxiality of strains and stresses in the neutron gauge volume (placed in the neck) is neglected. To prove that this assumption is reasonable, full macroscopic stress tensor has been estimated using FEA method. It was found that the triaxiality is actually negligible in the gauge volume measured by diffraction, i.e. the maximum stresses in TD and ND do not exceed 6.5% of the uniaxial stress applied in the rolling direction. This value is overestimated because the shape of the neck was taken just before fracture, when stress heterogeneity and triaxiality is maximal. Such argument is confirmed by measurements done using neutron diffraction in transverse direction with second detector bank (not presented here). Finally, in order to interpret experimental results, self-consistent modelling was performed assuming uniaxial tensile stress in the neutron gauge volume. The theoretical results can be then compared with the experimental stresses and strains averaged over the studied volume.

As shown in Fig. 4, the elastic lattice strains measured using different {hkl} reflection are correctly predicted by elastoplastic self-consistent model, up to large strain. Nevertheless, the only disagreement between elastoplastic model and experiment (i.e. decreasing of lattice strains for
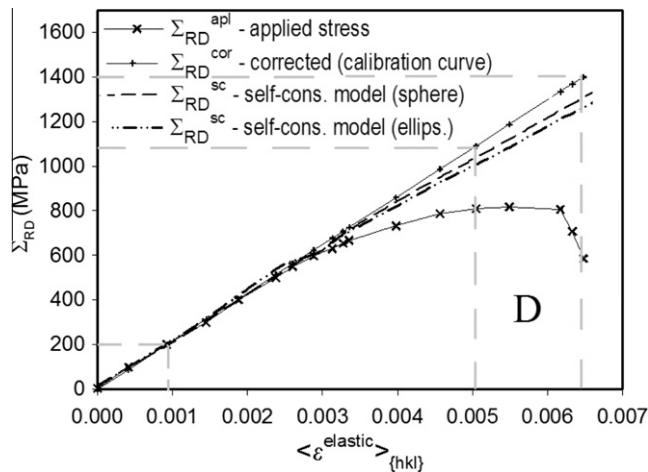

Fig. 3. Measured stress, calibrated stress and model stress versus the average of elastic lattice strains parallel $\langle \varepsilon_{RD} \rangle_{max}$ to the load direction (RD). In the calibration process, at each measured stress value corresponds a calibrated stress value on the linear corrected curve. Note that simulations performed for spherical and ellipsoidal inclusions in the self-consistent model lead to very similar results.
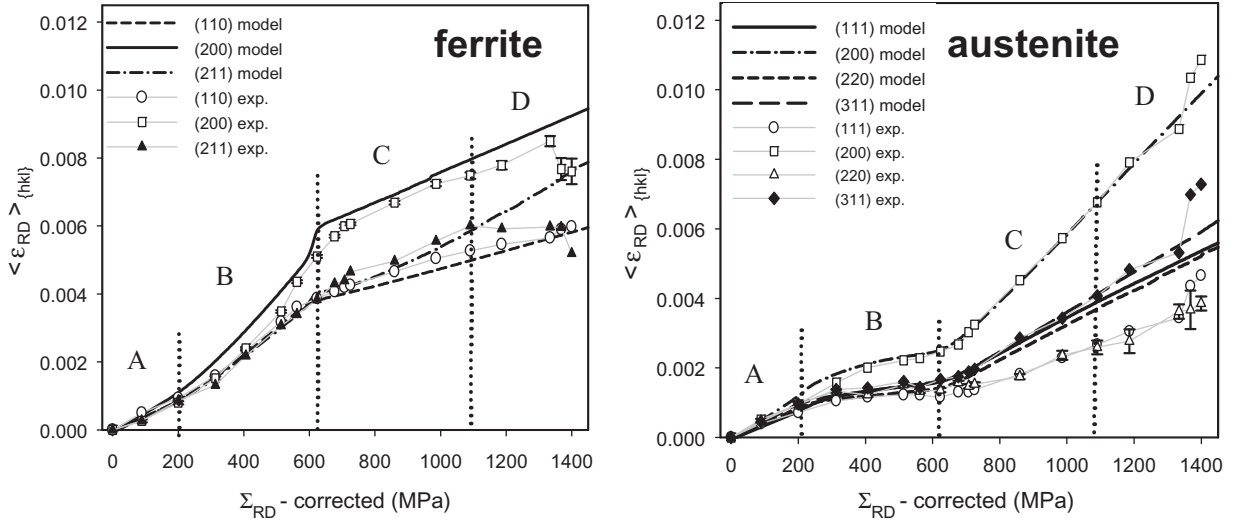
Fig. 4. Elastic lattice strains parallel $\langle\varepsilon_{RD}\rangle_{\{hkl\}}$ to the load direction (RD) versus corrected macroscopic stress $\sum_{RD}^{cor}$ for aged UR45 N samples deformed in tensile tests. Strains measured "in situ" for several {hkl} reflections in both phases (points) are compared with elastoplastic self-consistent model predictions (lines). Stages A, B, C, D corresponds respectively to elastic behaviour of both materials (A), elastic part for ferrite and linear plasticity for austenite (B), linear plasticity for both materials (C), other behaviors including damage (D). Self-consistent model is based on previous works (Baczmanski et al., 2003; Baczmanski and Braham, 2004). Calculations have been performed with a strain step of 0.1% and a number of 20000 grains.

{211} reflection in ferrite grains in Fig. 5) could be explained by mesoscopic damage process leading to relaxation of stresses for grains having specific orientations with respect to the specimen loading. Indeed, the SEM pictures on UR45 N steel show different mechanisms of such damage initiation, i.e. decohesion occurring along slip systems in ferritic phase or along interphase boundary due to stress concentration on inclusions present in the sample (Fig. 6). The first mechanism (decohesion on slip systems) could be responsible for relaxation of stresses for grains selected by the {2 1 1} reflection in ferritic phase. It should be stated that damage occurring from defects along slip systems in ferrite was already reported by Christian (1970), Vitek et al. (1970), Mahajan (1975), Louchet (1979), and

recently by Bugat (2000), where aged duplex steels were also studied using SEM method.

The fast decrease of lattice strains measured close to the sample fracture (see Fig. 4(a)) indicates that damage process seems occurring firstly in ferritic phase. When it relaxes significantly in ferrite, the applied load is transferred into austenite leading to an increase of measured lattice strains in the latter phase (as seen in Fig. 4(b)). To extract damage from our results, experiments can be compared with model predictions. As mentioned above, the theoretical data correspond to undamaged material because the calculations were performed with a purely elastoplastic model. On the other hand, the experimental results correspond to the real damaged material. The
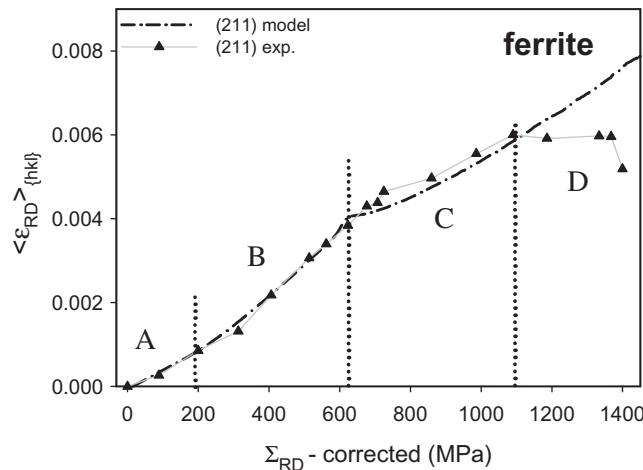

Fig. 5. Elastic lattice strains parallel $\langle\varepsilon_{RD}\rangle_{\{hkl\}}$ to the load direction (RD) versus corrected macroscopic stress $\sum_{RD}^{cor}$ for aged UR45 N samples deformed in tensile tests. Strains measured "in situ" for {2 1 1} reflection in the ferritic phase (points) are focused and compared with self-consistent model predictions (lines). Calculations have been performed with a strain step of 0.1% and a number of 20000 grains.
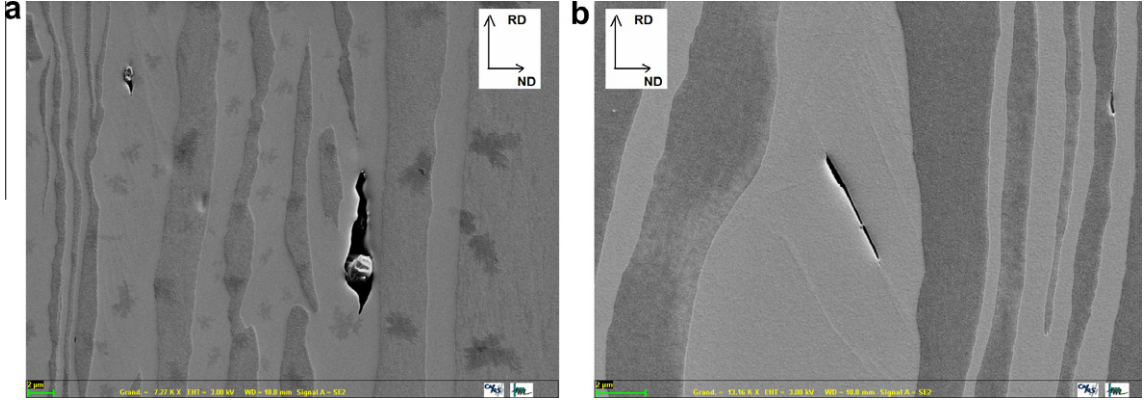
Fig. 6. Damage process caused by inclusions (a) and occurring on slip plane or at grain boundary (b) are shown in SEM pictures (ferritic phase is lighter than austenite one). The source of the contrast observed between the two phases corresponds to etching.

applied strain is the same for both experiment and simulation. In our analysis we assume that the damaged state can be related to the undamaged state. Thus using an energy equivalence principle, it can be demonstrated that (Saanouni, 1996; Lemaitre and Chaboche, 2001; Chaboche et al., 2006):

$$\sigma = \widetilde{\sigma} \times \sqrt{1 - \delta_{meso}}, \tag{2}$$

where $\widetilde{\sigma}$ is the effective stress corresponding to the undamaged material, i.e. the stress calculated with the self-consistent undamaged model; while σ is the real stress occurring in the damaged material and δ_{meso} is the mesoscopic damage, taken as a scalar parameter.

Assuming linear relation between stress and strain for elastic deformation, a similar equation can be written for the elastic lattice strain determined by neutron diffraction:

$$\langle \varepsilon_{RD}^{elastic} \rangle_{\{hkl\}exp} = \langle \varepsilon_{RD}^{elastic} \rangle_{\{hkl\}mod} \times \sqrt{1 - \delta_{\{hkl\}meso}}$$

$$\Longleftrightarrow \delta_{\{hkl\}meso} = 1 - \left(\frac{\langle \varepsilon_{RD}^{elastic} \rangle_{\{hkl\}exp}}{\langle \varepsilon_{RD}^{elastic} \rangle_{\{hkl\}mod}} \right)^2 \tag{3}$$

where $\langle \varepsilon_{RD}^{elastic} \rangle_{\{hkl\}exp}$ is the real elastic lattice strain determined by diffraction in damaged samples, $\langle \varepsilon_{RD}^{elastic} \rangle_{\{hkl\}mod}$ is an effective elastic strain in undamaged materials (calculated with the self-consistent model) and $\delta_{\{hkl\}meso}$ is the damage defined at mesoscopic scale, i.e. for the group of grains contributing to diffraction peak for $\{hkl\}$ reflection.

Applying the above formula to the results obtained with $\{2\,1\,1\}$ reflection (presented in Fig. 5), we can determine the evolution of damage versus macroscopic stress. The calculated points are presented in Fig. 7. It should be noted that for macroscopic stresses smaller than 1100 MPa, the values of $\delta_{\{hkl\}meso}$ obtained are randomly distributed around zero. Nonzero values of $\delta_{\{hkl\}meso}$ in this range come from discrepancies between experiment and model prediction (stages A, B and C in Fig. 5) and cannot be attributed to damage. Thus we can assume $\delta_{\{hkl\}meso} = 0$ for macroscopic stresses lower than 1100 MPa. However, significant increase of damage can be observed in Fig. 7, when the macroscopic stress value goes beyond this threshold value of 1100 MPa. The origin of such increase is the systematic deviation between measured and calculated stresses within the fourth stage D in Fig. 5.
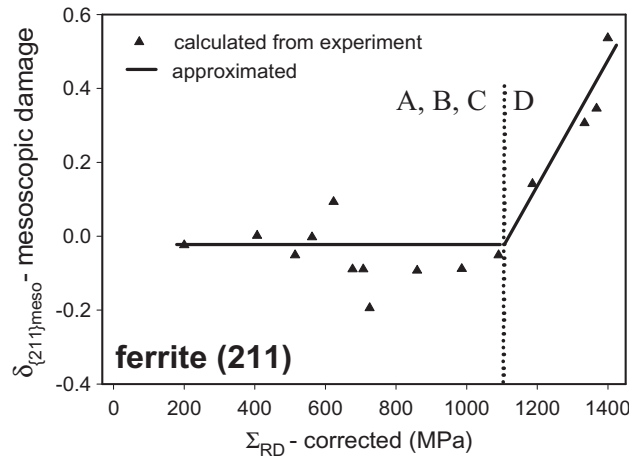

Fig. 7. Mesoscopic damage versus corrected macroscopic stress $\sum_{RD}^{cor}$ for aged UR45 N samples deformed in tensile tests. Damage calculated only for $\{2\,1\,1\}$ reflection in ferritic phase (points) is averaged by zero (lines) for small stresses because of experimental errors.

It can be concluded that the mesoscopic damage behaviour of studied duplex steel presents a threshold of stress at about 1100 MPa. A critical damage value can be identified at about 0.53 for a final macroscopic stress of about 1430 MPa. This latter corresponds to the macroscopic fracture of the specimen, probably due to micro cracks coalescence in ferrite. As previously stated, decohesion on crystallographic planes is one possible mechanisms initiating damage in ferritic phase. This phenomenon may occur only for specific orientations of slip systems with respect to the applied load. As shown in our analysis, the grains selected by the {2 1 1} reflection are the most sensitive to damage among all the observed reflections. Thus the methodology proposed in this work shows the possibility to extract selective damage at mesoscopic scale, thanks to neutron diffraction measurements.

4. Experimental methods at macroscopic scale

4.1. Geometrical correction of the stresses

Measurements at macroscopic scale have been also performed during mechanical tensile tests. The tensile machine is an Instron© 4484. Forces are measured by load cell with an accuracy of 1% of reading values. Strains are measured using an extensometer (accuracy of 0.15%). The principle of such a methodology is well known and it enables to obtain damage from hardening curves (Lemaitre and Chaboche, 2001). However in practical case, it is not possible to extract directly the macroscopic damage in a specimen. Indeed, for tensile tests with metallic materials, damage usually occurs at the same time as triaxial stress state due to necking phenomenon (plastic instability) causing a decrease in the cross-section area and thus an apparent softening. This particular problem can be solved by imaging the cross-section evolution during experiment. In the present study, pictures of the sample were taken with a rate of three pictures per second by double cameras system shown in Fig. 8. Examples of pictures taken by each camera and at different times are shown in Fig. 9. Using Matlab© software for images treatment, it is possible to measure the dimensions of the sample in each direction. Assuming that the cross-section is elliptical with axes along TD and ND, its area can then be calculated from the formula: $S = \pi R_1 R_2$, where R_1 and R_2 are the measured ellipse radii. The procedure has been done following previous studies (Cabezas and Celentano, 2004; Ostsemin, 2009). Experiment has been repeated twice on two different specimens, in order to check the repeatability. The final uncertainty of radii is between 0.05 and 0.15 mm and depends strongly on the camera resolution and the magnifying factor. The evolution of each radius is presented in Fig. 10. We can point out that the final radius value is very different for each camera, due to a very strong anisotropy of our studied duplex steel caused by crystallographic texture. Cross-section evolution with time is presented in Fig. 11. Three stages can be observed (Fig. 10 and 11). Stage α corresponds to quasi-constant cross-section during elastic behaviour of the material. Then a linear evolution stage, denoted by β, represents elastoplastic behaviour. Finally during stage γ a non-linear evolution of the cross-section has been observed. Such behaviour is expected when the material reaches the ultimate stress, then necking phenomenon occurs. Now, we can assume a model for section evolution and compare it with experimental results. In this paper, according to several authors (Lemaitre and Chaboche, 2001; Jaoul et al., 2008), we consider that the cross-section evolution can be described by the following equation:

$$S_E = S_0 \times \exp(-E_{cor}) \tag{4}$$

where S_E is the cross-section for a given strain state and S_0 is the cross-section at the initial state. If triaxiality and stress concentration are neglected, this formula allows direct correction of the macroscopic stress and it can be derived assuming incompressibility (constant volume) of the material during plastic deformation, until necking starts. E_{cor} is the corrected experimental macroscopic strain obtained using:
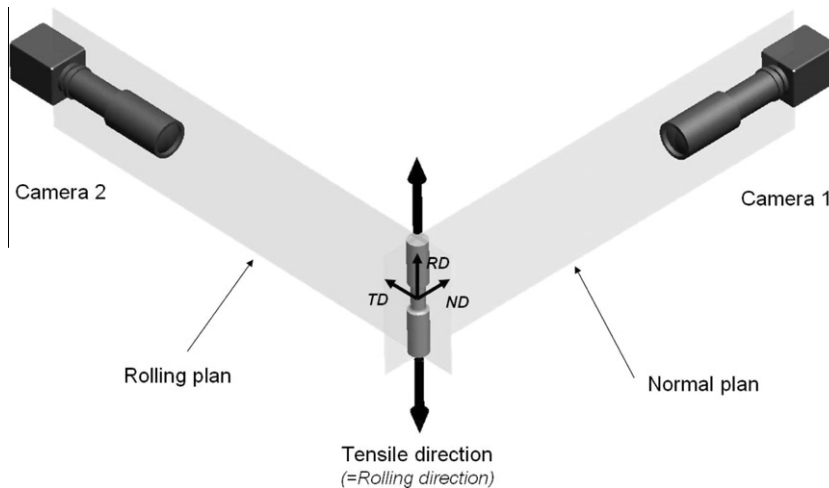

Fig. 8. Camera system description for imaging the cross-section and local strain during tensile tests.
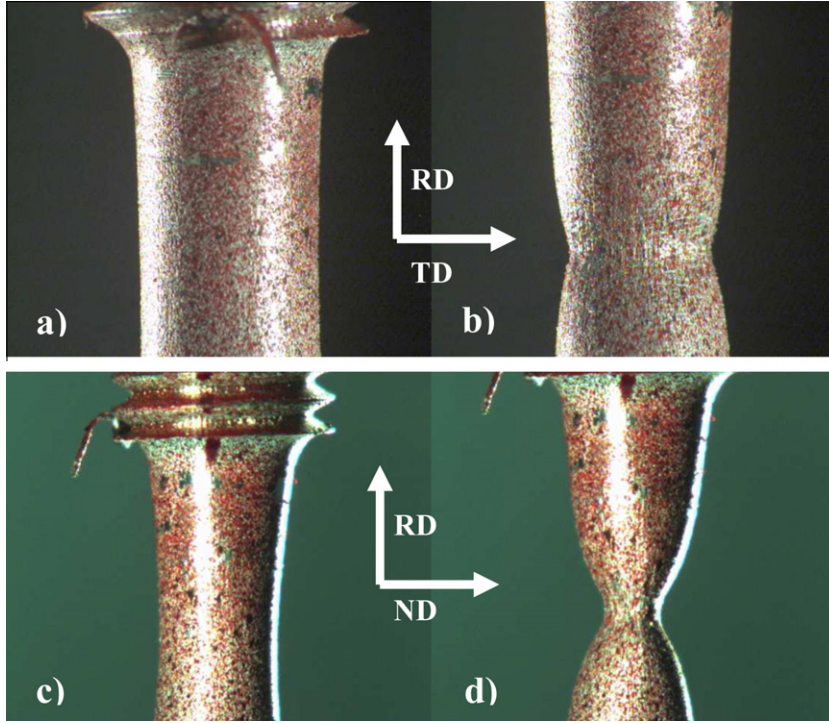
Fig. 9. Pictures from both cameras (a) and (b) for camera 1 and (c) and (d) for camera 2. Pictures (a) and (c) correspond to the beginning of the necking effect. Pictures (b) and (d) correspond to the end of the loading, close to the fracture time. "Pixels" on the pictures are due to speckle pattern treatment used for DIC calculations.
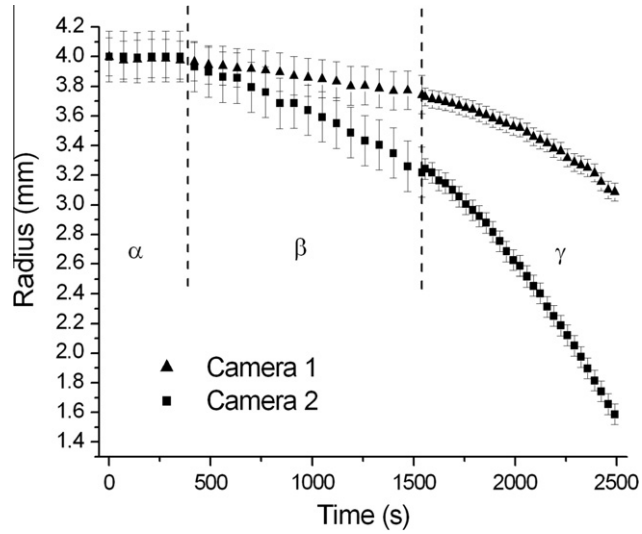

Fig. 10. Radius evolution in each direction perpendicular to the tensile loading versus the time. Three stages can be seen on these curves, denoted α, β, γ corresponding respectively to elastic, elastoplastic and elastoplastic with necking behaviour.

$$E_{cor} = \ln\left(1 + \frac{\Delta l}{l_0}\right) = \ln(1 + E_{exp}), \qquad (5)$$

where E_{exp} is the direct experimental macroscopic strain obtained from displacements Δl (measured with grips and/or extensometer). The comparison between experi-

mental and model cross-sections is shown in Fig. 11. For stages α and β, there is a perfect agreement between both curves. For large deformation corresponding to the stage γ, the model does not follow experimental result due to localisation of the strain, that has been not considered in theoretical calculation (Eq. (4)).
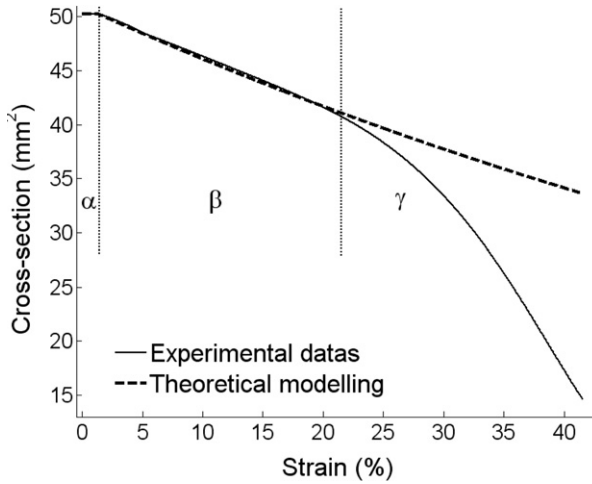
Fig. 11. Cross-section evolution during the tensile loading versus the time. Three stages can be seen on these curves, denoted α, β, γ corresponding respectively to elastic, elastoplastic and elastoplastic with necking behaviour. Full line corresponds to experimental measurements. Dash line corresponds to theoretical evolution of the cross-section.

4.2. Local deformation measurements

In order to extract damage from stress versus strain evolution, we have taken into account the cross-section evolution occurring for large deformation within the centre of our samples, and modifying the local stress. Therefore it is also necessary to obtain the correct strain values. In our experiments, the strain was measured using extensometer until 5.4%. Then, the extensometer was removed and the strain was calculated from the grips displacement of the tensile machine. However, for very large deformation, the strain is no longer uniform and the cross-section evolution versus the corrected experimental strain (E_{cor}) has no direct local meaning. In order to solve this problem, it can be possible to measure the local strain with ESPI (Guelorget et al., 2006, 2009) or by using digital image correlation (DIC) technique (Lu et al., 1997; Xu et al., 2008; Bornert et al., 2009). This latter has been used in the present paper. The DIC algorithm is based on image processing. Firstly, a speckle pattern was created on the specimen. As stated before, sample pictures were registered during tensile test by cameras, and the results were analysed using an open-source algorithm working in Matlab© (Eberl, 2006). Results are presented in Fig. 12 and compared with the global strain obtained from extensometer and grips displacement. Comparison shows that no difference is observed at small deformation, between axial strains (parallel to load direction) measured using both techniques. At about 25% and 77% of DIC strain, two thresholds of strain can be observed. This enables to distinguish again several stages in the studied curve, quoted by α, β, γ and δ. The first three correspond directly to those previously defined (Figs. 10 and 11), describing different behaviour of the material. Within the fourth stage δ, strain is increasing significantly. This stage occurs when the neck is already created and could be then linked to an apparent damage process. Differences between axial strains
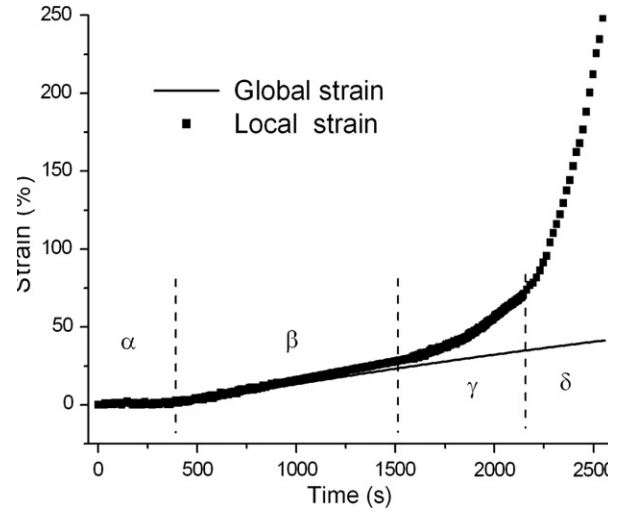

Fig. 12. Strain evolution during the tensile loading versus the time, using extensometer and grips displacement (global strain) or DIC technique (local strain) with average of camera 1 and 2 for both directions. Four stages can be seen on these curves, denoted α, β, γ and δ corresponding respectively to elastic, elastoplastic, elastoplastic with necking and strain quickening probably mixing damage processes and necking effect. The global strain corresponds to the machine strain. The local strain is a statistical average over several closer couples of points used to calculate the strain.

measured by camera 1 and camera 2 remain small and seem to correspond to errors on reference lengths used for DIC strain calculations. Correlation parameters are presented in Table 2. The final result is an average of these two values presented in Fig. 12. It can be outlined that local strain increases until 250%.

4.3. Elastoplastic modelling and parameters optimization

Knowing the local experimental strain evolution (E_{loc}) and the cross-section evolution within the necking area, it is now possible to plot the dependence of macroscopic stress as a function of macroscopic strain in the narrowest part of the neck. The results are presented in Fig. 13. In this graph is also reported the uncorrected stress versus global strain (cross points) and the corresponding results obtained during neutron diffraction at ISIS (square points). It shows a good agreement between both experiments. The dashed line, shown in Fig. 13, corresponds to the stress corrected only for evolution of the local cross-section versus global experimental strain (E_{cor}). As said before, this curve has no physical meaning because this strain is not corrected for localisation effects. Next curve (i.e. the dotted line) corresponds to the corrected stress versus the local strain determined using the DIC technique (E_{loc}), with an average of cameras 1 and 2. Comparison with the uncorrected curves indicates that local stress and local strain are the highest at the centre of the specimen. Indeed, the global measurements are still meaningful at large deformation: except the softening, they correspond to mechanical behaviour far from the necking zone, whereas the local curves correspond to real mechanical behaviour inside the necking zone.

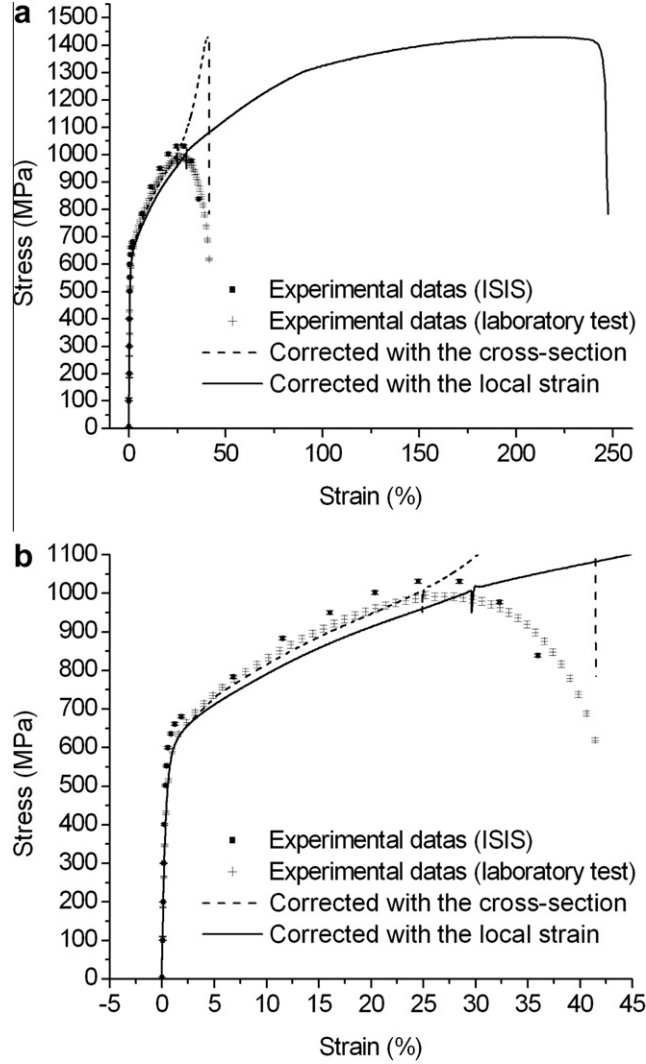| Parameters	Correlation surface (pixels²)	Correlation surface (mm²)	Distance between points used for local strain (mm)
Camera 1	20×20	0.62×0.62	0.23
Camera 2	20×20	0.66×0.66	0.25

Fig. 13. Stress versus strain: (a) whole curves, (b) magnifying part. Points correspond to uncorrected data from both experiences. The dash line corresponds to the corrected stress including evolution of the local cross-section versus global strain. The full line corresponds to the corrected stress versus the corrected local strain (from DIC technique).

In order to obtain damage evolution, it is necessary to compare experimental damage results with numerical undamaged modelling. This has been performed considering several macroscopic elastoplastic behaviour. Models have been chosen to take into account same phenomena as in the previous self-consistent modelling. Model 1 is a model using only isotropic hardening. This isotropic hardening is the Prandtl–Reuss non-linear model. It can be constructed on the following thermodynamics potentials (Lemaitre and Chaboche, 2001; Hfaiedh, 2009):

$$\rho_0 \psi = \frac{1}{2}\overline{E}^{el} : \overline{\overline{C}} : \overline{E}^{el} + \frac{M_Y}{M_Y + 1} Q \times r^{\frac{1}{M_Y}} + 1$$

$$\Phi = \overline{\overline{\sum}} : \frac{d\overline{E}^{pl}}{dt} - R\frac{dr}{dt} \geqslant 0$$

$$f = J_{II}\left(\overline{\sum}^D\right) - R - \sigma_Y$$

$$\Pi = -\Phi + \dot{\lambda} \times f,$$

$$(6)$$

where ψ is the Helmholtz specific free energy, ρ_0 is the initial density, $\overline{E}^{el}$ is the elastic part of the macroscopic

strain tensor, $\overline{E}^{pl}$ is the plastic part of the macroscopic strain tensor, $\overline{\sum}$ is the macroscopic stress tensor, $\overline{\overline{C}}$ is the four rank macroscopic elastic stiffness tensor, M_Y is the hardening exponent, Q is the hardening parameter, r is the isotropic hardening variable, R is the thermodynamics dual variable linked to r, Φ is the intrinsic dissipation, f is the yield function, J_{II} is the second invariant of the deviatoric stress tensor $\overline{\sum}^D$, $_Y$ is the initial yield stress, $\prod$ is the whole dissipation potential and $\dot{\lambda}$ is the plastic multiplier.

Model 2 is a model using isotropic hardening with a hardening exponent $M_Y = 1$, but considering an additional non-linear saturation term. It is based on the following thermodynamics potentials, studied in (Lemaitre and Chaboche, 2001; Hfaiedh, 2009):

$$\rho_0 \psi = \frac{1}{2} \overline{E}^{el} : \overline{\overline{C}} : \overline{E}^{el} + \frac{1}{2} Q \times r^2$$

$$\Phi = \overline{\sum} : \frac{d\overline{E}^{pl}}{dt} - R\frac{dr}{dt} \geq 0$$

$$f = J_{II}\left(\overline{\sum}^D\right) - R - \sigma_Y \qquad (7)$$

$$\Pi = -\Phi + \dot{\lambda} \times f + H(r)$$

$$H(r) = \frac{brR}{2} = \frac{bQr^2}{2} = \frac{bR^2}{2Q}.$$

The intrinsic dissipation Φ and the yield function f do not change. The Helmholtz specific free energy $\psi(\overline{E}^{el}, r)$ is now a quadratic form. $H(r)$ is a secondary potential corresponding to a secondary yielding surface and describing the hardening saturation, where b is the saturation parameter.

The previous models have been computed in Matlab©, for uniaxial loading. An inverse method has been performed to identify the modelling parameters with experimental data. The experimental curve corresponding to global behaviour has been optimized with such a methodology. Parameters for each model are summarized in Table 3. We can point out that both models give a difference for the parameters and especially for the yield stress. The results are presented in Fig. 14. Model 1 gives a better fitting at the beginning of plasticity because of the hardening exponent (1), whereas model 2 is better at the end because of the saturation parameter. The same approach has been done for the experimental curve corresponding to the local behaviour within the necking area. Because of the particular shape of this curve, only the second model can be used to obtain a convergent limit for the optimization. Parameters with model 2 are summarized in Table 3. The results are presented in Fig. 15. The model gives a good fitting up to large strains, which will allow us to extract different damage curves. Fig. 16 shows an example of an optimization error function obtained.

4.4. Macroscopic damage calculations and sensibility to elastoplastic modelling

As in the case of mesoscopic scale the damage process at macroscopic scale can be analysed comparing model calculations with experimental results. On one hand, the modelling results correspond to undamaged material

Table 3
Identification results for experimental curves.

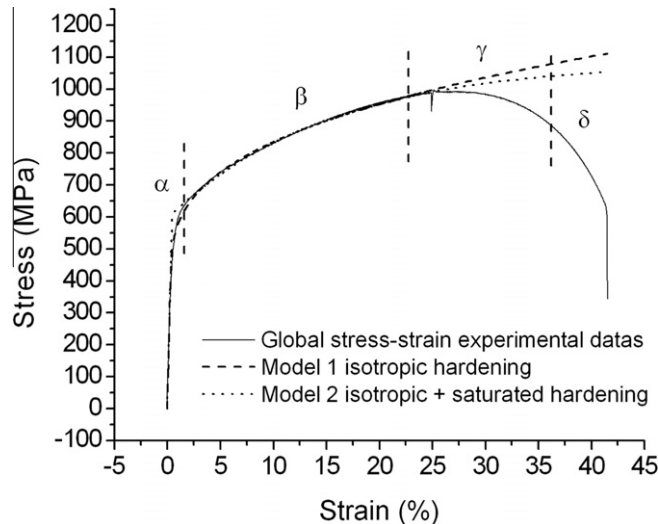| Parameters	Young modulus (GPa)	M_Y	Q (MPa)	σ_Y (MPa)	b
Model 1 with global stress-strain data	200	2.888	9.449E + 02	418.7	0
Model 2 with global stress-strain data	200	1	3.201E + 03	610.3	6.766
Model 2 with local stress-strain data	200	1	1.426E + 03	671.8	1.839

Fig. 14. Stress versus strain. Global experimental data compared with several modelling for macroscopic elastoplastic behaviour.
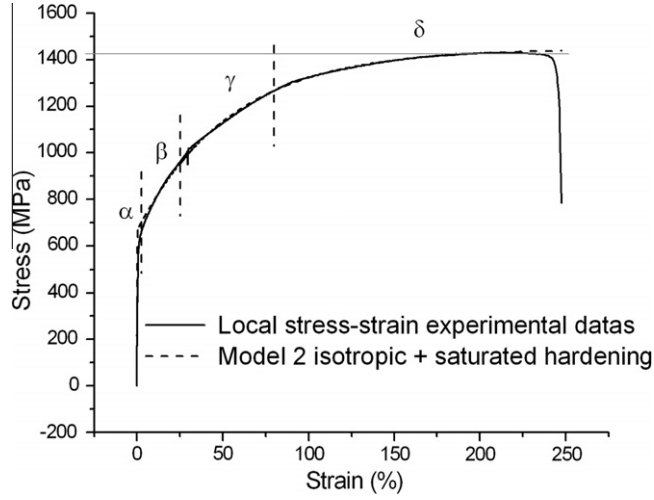
Fig. 15. Stress versus strain. Local experimental data compared with model 2, taking into account hardening saturation.
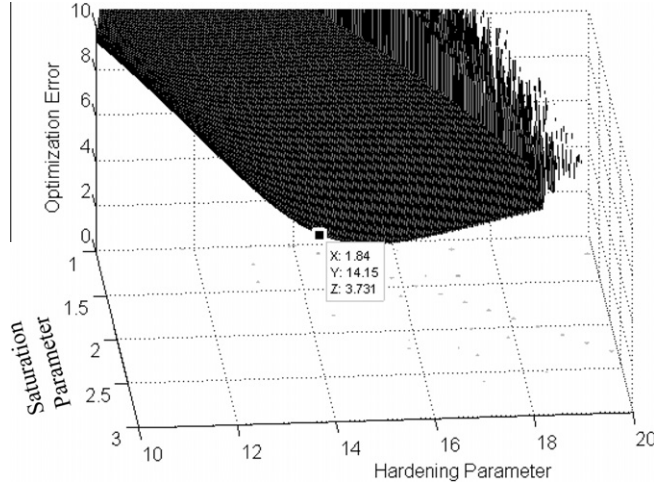

Fig. 16. Parameters optimisation for model 2, a global minimum has been found.

because they were computed with a purely elastoplastic model. On the other hand, the experimental data correspond to the real damaged material. The applied macroscopic strain is the same for both cases. Moreover, damaged state can be transformed theoretically to equivalent undamaged state. Once more, with an energy equivalence principle, the following equation can be used (Saanouni, 1996; Lemaitre and Chaboche, 2001; Chaboche et al., 2006):

$$\sum_{\text{exp}} = \widetilde{\sum}_{\text{mod}} \times \sqrt{1 - D_{macro}}, \qquad (8)$$

where $\widetilde{\sum}_{\text{mod}}$ is the effective macroscopic stress for the undamaged material, corresponding to the model stress, $\sum_{\text{exp}}$ is the macroscopic stress in the damaged material, corresponding to the measured stress. And D_{macro} is the macroscopic damage, taken as a scalar. This leads directly to the following useful formula:

$$D_{macro} = 1 - \left(\frac{\sum_{\text{exp}}}{\widetilde{\sum}_{\text{mod}}} \right)^2. \qquad (9)$$

Applying this relation to the macroscopic results, the macroscopic damage evolution versus macroscopic quantity can be found. The calculated points for global strain data are presented in Fig. 17(a). Mesoscopic results from ISIS experiment are superimposed. Whatever the models, the macroscopic damage has a very similar trend. Experimental uncertainties, calculated from the following formula, have been also reported in Fig. 17(b).

$$\Delta D_{macro} = 2 \times |1 - \min(D_{macro})| \times \frac{\Delta \sum_{\text{exp}}}{\left| \min\left(\sum_{\text{exp}} \right) \right|} \approx 0.02, \qquad (10)$$

where Δ means for the errors values. We can conclude that the macroscopic damage curve seems to be not very
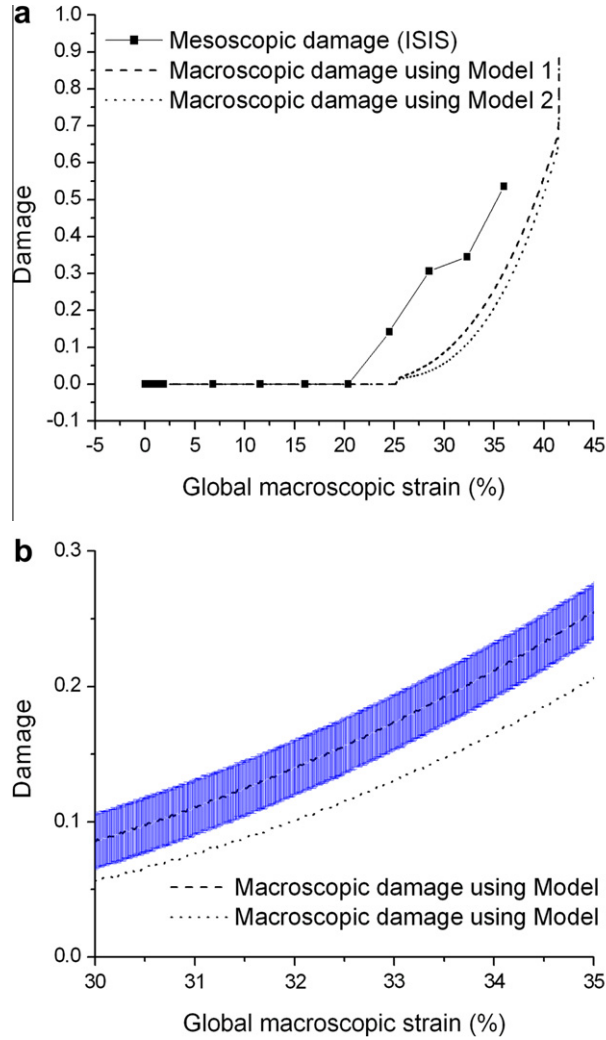
Fig. 17. Damage versus global macroscopic strain: (a) damage at mesoscopic scale (from ISIS experiments) and at macroscopic scale using both models, (b) magnifying part including errors.

sensitive to chosen models, i.e. it corresponds to a real physical damage behaviour.

Within the neck area, it is also possible to use the same procedure of damage determination. This calculus corresponds to local strain data and has been reported in Fig. 18. The local macroscopic damage behaviour of the studied duplex stainless steel presents a fuzzy threshold of strain within the necking area. However, a critical damage parameter can be identified at about 0.7 for a final strain of 247%. The threshold values corresponding to effective damage are quite different from stages obtained above from geometrical observations (Fig. 12). This can be explained through the quite complex necking effect which masks physical damage. During tensile experiment, several authors mention two stages of neck evolution: a diffuse necking and a localised necking (Considère, 1885). Stages γ and δ from Fig. 12 could correspond respectively to these two stages. Optical observations and DIC technique are only able to reveal a whole geometrical

contribution to the smoothing of the mechanical behaviour. Damage seems to be mainly effective within the stage δ.

5. Comparison between scales and discussion

Comparison between mesoscopic and macroscopic scales can also be done. To link Sections 3 and 4 more easily, different stages were marked and named as showed in Figs. 4, 5, 7, 11 and 12. At mesoscopic scale the evolution of measured elastic strains ($\langle \varepsilon_{RD} \rangle_{hkl}$) during tensile loading of the aged UR45 N sample can be divided into A, B, C and D ranges as shown in Figs. 4 and 5 (more details on the applied analysis are described in (Baczmański and Braham, 2004; Dakhlaoui et al., 2006). At the beginning (range A), both phases are below the yield point and linear elastic deformation occurs. Next, in the range B, a deviation from linearity appears in the axial strain data for both phases, approximately at the same stress level for all reflections,
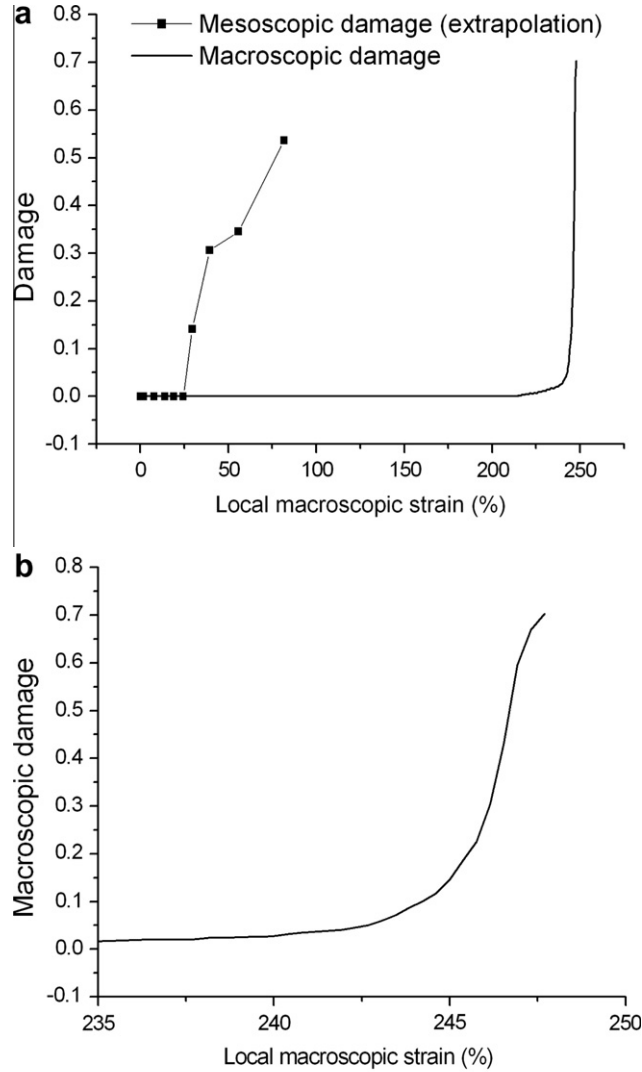
Fig. 18. Damage versus local macroscopic strain: (a) extrapolated damage at mesoscopic scale from ISIS measurements and effective damage at macroscopic scale occurring within the necking area, (b) magnifying part presenting only macroscopic damage.

indicating the beginning of plastic deformation in the austenitic phase. The elastic strains of austenite reflections increase more slowly than the elastic strains of ferrite reflections. Second important ranges (marked by C and D) are observed at a later stage of deformation, when all curves undergo again a significant gradient change indicating plastic deformation in the ferritic phase. Within the range C the dependence of $\langle \varepsilon_{RD} \rangle_{hkl}$ vs. applied stress $\sum_{RD}$ is approximately linear and confirmed by model prediction, while in D region disagreement between model and experiment occurs for the {2 1 1} reflection. Thus the range D is defined for the deformation in which the effects of damage are seen.

The α, β, γ, δ ranges marked in Figs. 10–12, 14 and 15 deal with macroscopic scale whose physical meanings have been explain above in this article. The α, β, γ parts correspond respectively to the same stages as A, B, C. However, the stage δ is not similar to the stage D, because

of difficulties to separate necking and damage at macroscopic scale. In order to make quantitative comparisons, two calibrations were made to avoid the necking influence on the macroscopic stress; it can be seen in Fig. 3 and Fig. 15 that maximal calibrated or corrected stresses are almost the same (1430 MPa) for both calibrations at the end of each tensile test. As stated above, some assumptions have been done. For example we consider no significant heterogeneity inside the neck meaning that stress concentration or triaxiality does not play a significant role. Another assumption deals with the choice of elastoplastic self-consistent model which has been used mostly to interpret results of diffraction experiments performed for small deformation.

In Fig. 17(a), the macroscopic damage behaviour extracted from curves uncorrected from necking phenomenon presents a threshold of strain at about 25.1%. Moreover a critical damage parameter can be identified at

about 0.9 for a final global strain of 41.5%. Whereas the mesoscopic damage behaviour of this duplex steel presents a threshold of strain at about 20.4%. Moreover a critical damage parameter can be identified at about 0.53 for a final strain of 35.9%. We see that span and shape of the both curves are quite the same, but the difference takes place with the threshold value. This could be explained by statistical difference between specimens used in different experiments (see Fig. 13(b) at macroscopic scale). The strain interval within the damage occurs is quite the same for both scales (ΔE = 15.5% at mesoscopic scale, ΔE = 16.4% at macroscopic scale). At grain scale, the damage in the {2 1 1} reflection of the ferrite phase occurs quite early. At macroscopic scale, the damage and the necking eventually seems to occur at the same time, certainly initiated by the mesoscopic {2 1 1} damage mechanism but resulting from an averaged damage in the underneath scale. So, comparison between mesoscopic and macroscopic scales show good agreements: mesoscopic damage seems to begin at the plan {2 1 1} just before first observation of effects at the macroscopic scale. As said before, because of the necking effect, the global strain does not lead directly to effective damage. It means that previous analysis is only qualitative. A quantitative measure of damage is shown in Fig. 18 (where δ_{meso} and D_{macro} are defined in Eqs. (3) and (9), respectively). According to the quite same behaviour between neutron (ISIS) and laboratory measurements at macroscopic scale (Fig. 13(b)), we assume the same behaviour at mesoscopic scale for each specimen used. This allows also plotting a corrected dependence of δ_{meso} (at mesoscopic scale) vs. local macroscopic strain within the neck, i.e. at large deformation (Fig. 18(a)). The most interesting result concerns the threshold value. Whatever the statistical difference between samples, we can conclude that mesoscopic damage along {2 1 1} slip system seem to take place earlier than macroscopic damage and does not contribute significantly to macroscopic behaviour of the sample, at the beginning. The cumulated damage from others slip systems occurs then only at the very end of the tensile test, what is confirmed by neutron diffraction (Fig. 4). The latter phenomenon is certainly responsible for the macroscopic failure of the sample.

6. Conclusion

In the present work, we have seen that it is possible to determine micromechanical effects of damage using neutron diffraction measurements. Methodology is quite efficient and easy due to the phase selectivity of the diffraction technique. Moreover, a comparison with macroscopic measurements has been done. Nevertheless, it is necessary to choose an elastoplastic model to interpret the obtained results. Two elastoplastic models have been performed with non-linear isotropic hardening. Comparison with the experimental data enables to identify parameters for each model, but not deciding the best one. This has been done for several experimental stresses versus strain curves (local and global). Errors have been also taken into account to analyse results from the different macroscopic models. Macroscopic damage evolution can then be calculated and compared with mesoscopic damage

obtained from neutron diffraction, especially for {2 1 1} reflection in DSS. Doing more accurate measurements at large deformation, it would be possible to determine damage effects to others reflections in ferrite, but probably also for austenitic phase. Then it could be possible to validate some micromechanical model including damage scales transition. The process used in the present paper is far from being perfect because some assumptions can be discussed. However, to our knowledge, it is the first attempt to extract damage from diffraction data and the first attempt to extract damage simultaneously at macroscopic and mesoscopic (grain) scales, in austeno-ferritic steels.

References

Amos, D., Eigenmann, B., Macherauch, E., 1994. Residual and loading stresses in two phase ceramics with different phase compositions. Z. Metallkd. 85 (5), 317–323.

Baczmański, A., Braham, C., 2004. Elastoplastic properties of duplex steel determined using neutron diffraction and self-consistent model. Acta Mater. 52, 1133–1142.

Baczmański, A., Wierzbanowski, K., Braham, C., Lodini, A., 1999. Arch. Metall. 44, 39–50.

Baczmański, A., Braham, C., Seiler, W., 2003. Microstresses in textured polycrystals studied by the multireflection diffraction method and self-consistent model. Philos. Mag. 83 (28), 3225–3246.

Baczmański, A., Dakhlaoui, R., Braham, C., Wierzbanowski, K., 2008. Examination of mechanical behavior of aged duplex steel using X-ray and neutron diffraction methods. Arch. Metall. Mater. 53, 89–96.

Bornert, M., Brémand, F., Doumalin, P., Dupré, J.-C., Fazzini, M., Grédiac, M., Hild, F., Mistou, S., Molimard, J., Orteur, J.-J., Robert, L., Surrel, Y., Vacher, P., Wattrisse, B., 2009. Assessment of digital image correlation measurement errors: methodology and results. Exp. Mech. 49, 353–370.

Bugat, S., 2000. Comportement et endommagement des aciers austéno-ferritiques vieillis, une approche micro-mécanique, PhD Thesis, ENSMP, Paris.

Cabezas, E., Celentano, D., 2004. Experimental analysis of the tensile test using sheet specimens. Finite Elem. Anal. Des. 40, 555–575.

Celentano, D.J., Chaboche, J.-L., 2007. Experimental and numerical characterization of damage evolution in steels. Int. J. Plasticity 23, 1739–1762.

Chaboche, J.-L., Boudifa, M., Saanouni, K., 2006. A CDM approach of ductile damage with plastic compressibility. Int. J. Fracture 137, 51–75.

Chehab, B., Bréchet, Y., Véron, M., Jacques, P.-J., Parry, G., Mithieux, J.-D., Glez, J.-C., Pardoen, T., 2010. Micromechanics of high-temperature damage in dual-phase stainless steel. Acta Mater. 58, 626–637.

Christian, J.W., 1970. Plastic deformation of BCC metals. In: Second International Conference on the Strength of Metals and Alloys.

Clausen, B., Lorentzen, T., Bourke, M.A.M., Daymond, M.R., 1999. Mater. Sci. Eng. A. 259, 17–24.

Considère, A., 1885. Mémoire sur l'emploi de fer et de l'acier dans les constructions. Annales des Ponts et Chaussées 9, 574–775.

Courant, B., Bourniquel, B., François, M., Bessière, M., 2000. Observations on two commonly used profile shape functions. Mater. Sci. Forum 347 (3), 161–165.

Dakhlaoui, R., Baczmański, A., Braham, C., Wronski, S., Wierzbanowski, K., Oliver, E.C., 2006. Acta Mater. 54, 5027–5039.

Eberl, C., Thompson, R., Gianola, D., 2006. Digital Image Correlation and Tracking. <http://www.mathworks.com/matlabcentral/fileexchange/12413>.

Fitzpatrick, M.E., Hutchings, M.T., Withers, P.J., 1997. Acta Mater. 45, 4867–4876.

François, M., Bourniquel, B., Not, C., Guillén, R., Duval, C., 2000. Parameters influencing peak localization repeatability for X-ray stress measurements – use of experiment designs technique. Zeitschrift Für Metallkunde 91 (5), 414–420.

Fréour, S., Gloaguen, D., François, M., Guillén, R., Girard, E., Bouillo, J., 2002. Determination of the macroscopic elastic constants of a phase embedded in a multiphase polycrystal – application to the beta-phase of a Ti–17 titanium based alloy. Mater. Sci. Forum 404 (7), 723–728.

Fréour, S., Gloaguen, D., François, M., Guillén, R., 2003. Modeling and simulation of multi-phase effects on X-ray elasticity constants. Phys. Status Solidi B 239 (2), 297–309.

Fréour, S., Gloaguen, D., François, M., Perronnet, A., Guillén, R., 2005. Determination of Single Crystal elasticity constants in a cubic phase within a multiphase alloy – X-ray diffraction measurements and inverse scale transition modelling. J. Appl. Crystallogr. 38, 30–37.

Gloaguen, D., François, M., Guillén, R., Royer, J., 2002a. Evolution of internal stresses in rolled Zr702. Acta Mater. 50 (4), 871–880.

Gloaguen, D., François, M., Guillén, R., Royer, J., 2002b. Interpretation of X-ray stress measurement and evaluation of internal residual stresses in rolled a-Ti40 using self-consistent models. Phys. Status Solidi A. 193 (1), 12–25.

Greenough, G.B., 1949. Residual lattice strains in plastically deformed polycrystalline metal aggregates. Proc. R. Soc. London A., 556–567.

Guelorget, B., François, M., Vial-Edwards, C., Montay, G., Daniel, L., Lu, J., 2006. Strain rate measurement by electronic speckle pattern interferometry: a new look at the strain localization onset. Mater. Sci. Eng. A 415, 234–241.

Guelorget, B., François, M., Montay, G., 2009. Strain localization band width evolution by electronic speckle pattern interferometry strain rate measurement. Scripta Mater. 60, 647–650.

Hedström, P., Han, T.-S., Lienert, U., Amer, J., Odén, M., 2010. Load partitioning between single bulk grains in a two-phase duplex stainless steel during tensile loading. Acta Mater. 58, 734–744.

Hfaiedh, N., 2009. Modélisation micromécanique des polycristaux – couplage plasticité, texture et endommagement, PhD Thesis, UTT, Troyes.

Hutchings, M.T., Withers, P.J., Holden, T.M., Lorentzen, T., 2005. Introduction to the Characterization of Residual Stress by Neutron Diffraction. CRC Press, Taylor and Francis, London.

Jaoul, B., Friedel, J., Crussard, C., 2008 (Etude de la plasticité et application aux métaux). Presses de l'Ecole des Mines, France.

Lacombe, P., Baroux, B., Béranger, G., 1990. Les aciers inoxydables, Les éditions de physique. Les Ulis, Berlin.

Lagneborg, R., 1967. Acta Metall. 15, 1737.

Le Joncour, L., Panicaud, B., Baczmański, A., Francois, M., Braham, C., Paradowska, A., 2010. Large deformation and mechanical effects of damage in aged duplex stainless steel. Mater. Sci. Forum 652, 155–160.

Lemaitre, J., Chaboche, J.-L., 2001. Mécanique des matériaux solides, second ed. Dunod, France.

Lipinski, P., Berveiller, M., 1989. Elastoplasticity of micro-inhomogeneous metals at large strains. Int. J. Plasticity 5, 149–172.

Louchet, F., 1979. Plasticité des métaux de structure cubique centrée. In: Dislocations et déformation plastique, France.

Lu, H., Vendroux, G., Knauss, W.G., 1997. Surface deformation measurements of a cylindrical specimen by digital image correlation. Exp. Mech. 37 (4), 433–439.

Mahajan, S., 1975. Interrelationship between slip and twinning in BCC crystals. Acta Metall. 23, 671–684.

Marcinkowski, M.J., Fischer, R.M., Szirmae, A., 1964. Trans. Metall. Soc. AIME 230, 676–689.

Mateo, A., Llanes, L., Anglada, M., Redjaimia, A., Metauer, G., 1997. J. Mater. Sci. 32, 4533–4540.

Ostsemin, A.A., 2009. On the analysis of stress state in elliptical tensile neck. Strength Mater. 41 (4), 356–362.

Park, C.J., Kwon, H.S., 2002. Corros. Sci. 44, 2817–2830.

Pecharsky, P., Vitalij, K., Zavalij, Y., 2008. Fundamentals of powder diffraction and structural characterization of materials. Springer.

Quinta Da Fonseca, J., Oliver, E.C., Bate, P.S., Withers, P.J., 2006. Mater. Sci. Eng. A. 437, 26–32.

Saanouni, K., 1996. Micromechanical modelling of low cycle fatigue under complex loadings. Part1: theoretical formulation. Int. J. Plasticity 12, 1111–1121.

Saanouni, K., Hammi, Y., 2000. Numerical simulation of damage in metal forming processes. Contin. Damage Fracture, 353–363.

Saanouni, K., Nesnas, K., Hammi, Y., 2000. Damage modelling in metal forming processes. Int. J. Damage Mech. 9, 196–240.

Santisteban, J., James, J., Daymond, M., Edwards, L., 2006. J. Appl. Crystallogr. 39, 812–825.

Vitek, V. et al., 1970. The core structure of ½⟨1 1 1⟩ screw dislocations in BCC crystals. Philos. Mag. 21, 1049–1073.

Wierzbanowski, K., Jura, J., Haije, W.G., Helmholdt, R.B., 1992. Cryst. Res. Technol. 27, 513–522.

Xu, Z.-H., Li, X.-D., Sutton, M.-A., Li, N., 2008. Drift and spatial distortion elimination in atomic force microscopy images by digital image correlation technique. J. Strain Anal. 43, 729–743.